

Dalton Transactions

Accepted Manuscript



This is an *Accepted Manuscript*, which has been through the Royal Society of Chemistry peer review process and has been accepted for publication.

Accepted Manuscripts are published online shortly after acceptance, before technical editing, formatting and proof reading. Using this free service, authors can make their results available to the community, in citable form, before we publish the edited article. We will replace this *Accepted Manuscript* with the edited and formatted *Advance Article* as soon as it is available.

You can find more information about *Accepted Manuscripts* in the [Information for Authors](#).

Please note that technical editing may introduce minor changes to the text and/or graphics, which may alter content. The journal's standard [Terms & Conditions](#) and the [Ethical guidelines](#) still apply. In no event shall the Royal Society of Chemistry be held responsible for any errors or omissions in this *Accepted Manuscript* or any consequences arising from the use of any information it contains.

Understanding the contribution of hydroxyl to energy band of semiconductor: $\text{Bi}_2\text{O}(\text{OH})_2\text{SO}_4$ vs. $\text{Bi}_6\text{S}_2\text{O}_{15}$

Juan Xu¹, Fei Teng^{1*}, Yunxuan Zhao¹, Yandong Kan¹, Liming Yang¹, Yang Yang¹,
Wenqing Yao², Yongfa, Zhu²

¹*Jiangsu Engineering and Technology Research Center of Environmental Cleaning Materials (ECM), Jiangsu Key Laboratory of Atmospheric Environment Monitoring and Pollution Control (AEMPC), Jiangsu Joint Laboratory of Atmospheric Pollution Control (APC), Collaborative Innovation Center of Atmospheric Environment and Equipment Technology (AEET), School of Environmental Science and Engineering, Nanjing University of Information Science & Technology, 219 Ningliu Road, Nanjing 210044, China.*

²*Department of Chemistry, Tsinghua University, Beijing 100082, China.*

Abstract

It is still big challenge to facilely tune the energy bands of semiconductor. Herein, we have mainly investigated energy bands and photochemical properties of $\text{Bi}_6\text{S}_2\text{O}_{15}$ and $\text{Bi}_2\text{O}(\text{OH})_2\text{SO}_4$, which have the very similar layered structure. It is found that the hydroxyl have down shifted the conduction band (CB, 0.21 eV) and valence band (VB, 4.39 eV) of $\text{Bi}_2\text{O}(\text{OH})_2\text{SO}_4$, compared with those (CB=0 eV; VB=3.36 eV) of $\text{Bi}_6\text{S}_2\text{O}_{15}$. Moreover, the main oxidative species over $\text{Bi}_6\text{S}_2\text{O}_5$ and $\text{Bi}_2\text{O}(\text{OH})_2\text{SO}_4$ are holes (h^+) and

* Corresponding author. Tel./Fax.: +86-25-58731090; Email address: tfwd@163.com

hydroxyl radicals ($\bullet\text{OH}$) for the degradation of rhodamine B (RhB) dye, respectively. This obvious difference has been mainly attributed to the hydroxyl, which have changed energy band structure and band gap. In addition, we have also investigated the morphology-dependent properties of $\text{Bi}_2\text{O}(\text{OH})_2\text{SO}_4$. Under ultraviolet light irradiation ($\lambda \leq 420$ nm), $\text{Bi}_2\text{O}(\text{OH})_2\text{SO}_4$ microspheres show an activity 1.3 times and 2.2 times higher than long flakes and straw sheaves for the degradation of (RhB), respectively. This study provides us a new idea that we can facilely tune energy band of semiconductor by introducing or removing hydroxyl or the other anions.

Keywords: Hydroxyl; Energy band; $\text{Bi}_2\text{O}(\text{OH})_2\text{SO}_4$; $\text{Bi}_6\text{S}_2\text{O}_{15}$

1. Introduction

Up to now, the practical applications of photocatalysis technology are greatly limited by the low quantum efficiency, light utilization efficiency and photo-activity. Specifically, the low photochemistry activities for most of visible light and near-infrared light responsive semiconductors and the low utilization of solar energy for ultraviolet light responsive ones are still big challenges for photocatalysis technology. Thus, it is desirable to obtain excellent photocatalysts with both a high utilization of solar energy and high quantum efficiency simultaneously. On base of BiPO_4 ¹ and Ag_3PO_4 ²⁻⁴ as the efficient photocatalysts, we could expect that oxyacid salts can be potentially developed as new photocatalysts through intercalation of anions containing p-block nonmetals (e.g., B, P, S, etc.) in binary oxide (e.g., Bi_2O_3 , Cu_2O , etc.), for example, $\text{Bi}_3\text{O}_4\text{Cl}$,⁵ $\text{Bi}_2\text{O}_2\text{CO}_3$,⁶ etc. In these cases, the featured layered structures are reported to produce an internal electric field that is favorable for the efficient charges separation and transfer. These oxyacid salts have been demonstrated to have high photoactivities. Moreover, the hydroxyl-containing compounds with positive valence bands also have excellent photodegradation abilities for organic pollutants, for example, $\text{ZnSn}(\text{OH})_6$,⁷ $\text{In}(\text{OH})_3$,⁸ $\text{CaSbO}(\text{OH})_3$,⁹ $\text{Bi}_2\text{O}_2(\text{OH})(\text{NO}_3)$ ¹⁰ etc. It has been reported that their positive valence bands not only endow the photogenerated holes with a strong oxidizing ability that leads to the complete mineralization of organic pollutants, but also facilitate to form the reactive hydroxyl radicals by exciting the abundant surface OH ($E^\circ(\bullet\text{OH}/\text{OH}^-) = 2.38 \text{ eV}$). In

addition, it has been reported¹¹ that sulfate-modified TiO₂ has also shown an increased photodecomposition rate, which has been ascribed to both a strong bonding ability of sulfate anion with H₂O and a high drawing force for holes by the negative charged sulfate anion. In our previous study,¹² we have demonstrated Bi₂O(OH)₂SO₄ as a potential new photocatalyst by theory calculation. However, to the best of our knowledge, there is no extensive study on morphology control of Bi₂O(OH)₂SO₄.

Herein, Bi₂O(OH)₂SO₄ with well-controlled morphology has been achieved by a simple and mild hydrothermal method. Firstly, we demonstrate the influences of temperature, reaction medium, pH, the addition amount of SO₄²⁻ ion added on the shapes of Bi₂O(OH)₂SO₄ samples. Our studies show that, by tuning appropriate reaction parameters, Bi₂O(OH)₂SO₄ with different shapes, grain sizes, and structures can be controllably synthesized. Secondly, we have investigated the morphology-dependent photocatalytic activity for the degradation of rhodamine B (RhB). Moreover, the effect of hydroxyl on crystal structure, electronic and band structures and photocatalytic activity is also investigated. It is interesting that the main oxidative species transform from holes (h⁺) to the hydroxyl radicals (•OH) due to the induction of hydroxyl. The tuning strategy is useful and promising, although the activity of Bi₂O(OH)₂SO₄ is not higher than that of Bi₂O(OH)₂SO₄. This study provides us a new idea that we can facilely tune energy band of semiconductor by introducing or removing hydroxyl or the other anions so as to develop new photocatalysts. For example, most of visible light responsive photocatalysts (*e.g.*, Fe₂O₃, CuO, etc.) usually have lower photochemistry activities than ultraviolet light

responsive ones. In particular, near-infrared light responsive semiconductors have fairly low or even have no photocatalytic activity (e.g., $\text{Cu}(\text{OH})\text{PO}_4$), which limits the utilization of solar energy. We can introduce hydroxyl or the other suitable anions to adjust appropriate energy bands of visible light responsive photocatalysts to develop a new photocatalyst with an improved activity; besides, for ultraviolet light responsive photocatalysts, the low utilization of solar energy is very low, which limits the practical application. We can remove anion from the appropriate anion to reduce band gap to develop new visible light responsive photocatalyst.

2. Experimental section

2.1. Sample preparation

All reagents were of analytical grade, purchased from Beijing Chemical Reagents Industrial Company of China, and were used without further purification. A simple hydrothermal method was used to prepare the samples.

Preparation of $\text{Bi}_2\text{O}(\text{OH})_2\text{SO}_4$ straw sheaves. Typically, 1 mmol $\text{Bi}(\text{NO}_3)_3 \cdot 5\text{H}_2\text{O}$ was firstly dissolved in 15 mL ethylene glycol (EG) and 15 mL distilled water. Then 1 mmol Na_2SO_4 was added to the solution above. After stirring for 30 min, the solution was transferred into a 40 mL Teflon-lined stainless steel autoclave, and was then heated at 90 °C for 24 h. After the hydrothermal treatment, the autoclave was cooled to room temperature naturally. Sequentially, a white precipitate was collected by centrifuging, and washed with distilled water and ethanol three times. Finally, the sample was dried in an oven at 60 °C for 5 h.

Preparation of $\text{Bi}_2\text{O}(\text{OH})_2\text{SO}_4$ long flakes. The same procedures were used except that EG was replaced by ethanol.

Preparation of $\text{Bi}_2\text{O}(\text{OH})_2\text{SO}_4$ microspheres. The same procedures were used except that the amount of Na_2SO_4 added was varied from 1 mmol to 0.67 mmol.

Preparation of $\text{Bi}_6\text{S}_2\text{O}_5$. In a typical procedure, 0.67 mmol Na_2SO_4 and 2 mmol $\text{Bi}(\text{NO}_3)_3 \cdot 5\text{H}_2\text{O}$ (1:3 molar ratio) were added into 30 mL of distilled water, and then 0.5 mL of 25~28 wt.% $\text{NH}_3 \cdot \text{H}_2\text{O}$ were added to the mixture above. The resulting precursor suspension was magnetically stirred for 30 min at room temperature and then transferred into a 40 ml Teflon -lined stainless steel autoclave. The autoclave was sealed and maintained at 180 °C for 24 h in an oven. After 24 h, the autoclave was

cooled to room temperature naturally. The white precipitate was washed with distilled water three times and dried at 60 °C in air.

2.2. Characterization

The crystal structures of the samples were determined by X-ray powder polycrystalline diffractometer (Rigaku D/max-2550VB), using graphite monochromatized Cu K radiation ($\lambda = 0.154$ nm), operating at 40 kV and 50mA. The XRD patterns were obtained in the range of 20-80° (2θ) at a scanning rate of 7 ° min⁻¹. The samples were characterized on a scanning electron microscope (SEM, Hitachi SU-1510) with an acceleration voltage of 15 keV. The samples were coated with 5-nm-thick gold layer before observations. The fine surface structures of the samples were determined by high-resolution transmission electron microscopy (HRTEM, JEOL JEM-2100F) equipped with an electron diffraction (ED) attachment with an acceleration voltage of 200 kV. UV-vis diffused reflectance spectra (UV-DRS) of the samples were obtained using a UV-vis spectrophotometer (UV-2550, Shimadzu, Japan). BaSO₄ was used as a reflectance standard in a UV-vis diffuse reflectance experiment. The photoluminescence (PL) spectra were obtained on Cary Eclipse fluorescence spectrophotometer at room temperature. The PL lifetime was measured using time-resolved fluorescence decay spectra by time-correlated single-photon counting under the 260 nm laser excitation (Cary Eclipse, Agilent). Nitrogen sorption isotherms were performed at 77 K and < 10⁻⁴ bar on a Micromeritics ASAP2010 gas adsorption analyzer. Each sample was degassed at 150 °C for 5 h before measurements. Surface area was calculated by the Brunauer-Emmett-Teller (BET)

method.

2.3. Transient photocurrents and electrochemical impedance spectroscopy (EIS)

An electrochemical system (CHI-660B, China) was employed to measure the photocurrents and electrochemical impedance spectroscopy (EIS). Electrochemical impedance spectroscopy (EIS) was performed from 0.1 Hz to 100 kHz at an open circuit potential of 0.3 V and an alternating current (AC) voltage amplitude of 5 mV. The data were analyzed by ZSimWin software. Photocurrent measurements were carried out in a conventional three-electrode system, in which indium-tin oxide (ITO) glass was used as the current collector to fabricate photo electrode, and 0.1 M Na₂SO₄ was used as the electrolyte solution. Bi₆S₂O₁₅/ITO and Bi₂O(OH)₂SO₄/ITO photo electrode were prepared by a coating method.

2.4. Evaluation of photocatalytic activity

The photo catalytic activity of the sample was evaluated by the degradation of rhodamine B (RhB) aqueous solution under UV light ($\lambda \leq 420$ nm), using a 300 W Xe arc lamp (CEL-HXF 300) equipped with an ultraviolet cutoff filter as a light source. The reaction system was placed in a sealed black box with the top opened, and was maintained a distance of 15 cm from the light source. The photocatalysts (100 mg) were dispersed in 200 mL of 10 mg/L RhB aqueous solution in a Pyrex beaker at room temperature. Before lighting on, the suspension was continuously stirred for 30 min in the dark to ensure the establishment of an adsorption–desorption equilibrium between the catalysts and RhB solution. During degradation, 3 mL of solution was

collected by pipette at an interval of irradiation, and subsequently centrifuged to remove the catalysts. UV-vis absorption spectra were recorded on a Spectrumlab 722sp spectrophotometer to determine the concentration of RhB. The degradation reaction could be expressed by an apparent first-order rate constant (k_a), which could be calculated using the following equation:

$$\ln(C_0/C) = k_a \times t, \text{ or } C = C_0 \times \exp(-k_a \times t) \quad (1)$$

where C_0 is the initial concentration of RhB solution, and C is the concentration of RhB at t -min irradiation, respectively. The active species generated in the photocatalytic reaction were detected through trapping experiments, in which 10 mL dimethyl sulfoxide (DMSO) and 1 mmol ammonium oxalate ((NH₄)₂C₂O₄) were used as hydroxyl radicals scavenger and holes scavenger, respectively.

2.5. Theoretical calculation

The simulated results of band structures, total and partial densities of states (DOS) were calculated by density functional theory (DFT) as implemented in the CASTEP. The calculations were carried out using the generalized gradient approximation (GGA) level, and Perdew-Burke-Ernzerh (PBE) formalism for combination of exchange and correlation function. The cut-off energy is chosen as 380 eV, and a density of (3×2×5) Monkhorst-Pack K-point were adopted to sample the Brillouin zone.

3. Results and discussion

3.1 Bi₂O(OH)₂SO₄ vs. Bi₆S₂O₁₅: Role of hydroxyl:

3.1.1 Effect on crystal structure

In order to understand the role of hydroxyl, Bi₆S₂O₁₅ nanowires are prepared and compared Bi₂O(OH)₂SO₄ microspheres, in which no hydroxyl is contained. The surface morphologies and particle sizes of Bi₆S₂O₁₅ and Bi₂O(OH)₂SO₄ were observed by scanning electron microscope (SEM). Fig. S1a shows that the Bi₆S₂O₁₅ products are composed of nanowires with diameter about 60 nm and the length more than tens of micrometers. The SEM micrographs of Bi₂O(OH)₂SO₄ were illustrated in Fig. S1b. It reveals that products of Bi₂O(OH)₂SO₄ consist of uniform microspheres with the diameters of 20-25 μm. The X-ray diffraction (XRD) patterns of Bi₆S₂O₁₅ and Bi₂O(OH)₂SO₄ are presented in Fig. S2a and b, respectively. Fig. S2a shows the diffraction peaks of Bi₆S₂O₁₅ are in agreement with the previous report of Bi₆S₂O₁₅ nanowires.¹³ The XRD patterns of Bi₂O(OH)₂SO₄ are shown in Fig. S2b. All the diffraction peaks are in good agreement with the standard card (JCPDS 76-1102). No impurities peaks, e.g., Bi(OH)₃ or Bi₂O₃ or Bi, are observed, which confirms the formation of phase-pure Bi₆S₂O₁₅ and Bi₂O(OH)₂SO₄. Fig. 1a shows the crystal structure of Bi₆S₂O₁₅ with the unit cell parameters of $a = 12.206(1) \text{ \AA}$, $b = 19.611(2) \text{ \AA}$, $c = 5.8388(7) \text{ \AA}$.¹³ The unit cell of Bi₆S₂O₁₅ is (Bi₁₂O₁₄)_n⁸ⁿ⁺ columns extending alone the c axis, which are surrounded by eight tetrahedral SO₄²⁻.¹⁴ Two different Bi can be

found in a unit cell: the $[\text{BiO}_6]$ unit with only Bi-O-Bi bonds, and $[\text{BiO}_3]$ unit with Bi-O-Bi and Bi-O-S bonds. Fig. 1b presents the super cell of $\text{Bi}_2\text{O}(\text{OH})_2\text{SO}_4$, which has a monoclinic space $P21/c$ with the unit cell parameters of $a = 7.692(3) \text{ \AA}$, $b = 13.87(1) \text{ \AA}$, $c = 5.688(2) \text{ \AA}$, and $\beta = 109.01(3)^\circ$.¹² It consists of sulfate anions and infinite $[\text{Bi}_2\text{O}(\text{OH})_2^{2+}]_n$ double chains, with a featured layered structure. It is observed that each hydroxyl (OH) connects two Bi atoms, and each O atom connects three Bi atoms. In this case, the induction of hydroxyl (OH^-) has changed the crystal structure, which may have an effect on the photocatalytic activity. And this will be further discussed in the following.

3.1.2 Effect on optical property

Fig. 2 displays the UV-vis diffuse reflectance absorption spectra (DRS) of the as-prepared $\text{Bi}_6\text{S}_2\text{O}_{15}$. It can be observed that $\text{Bi}_6\text{S}_2\text{O}_{15}$ exhibits optical absorption in UV ranges. The band gap energy of $\text{Bi}_6\text{S}_2\text{O}_{15}$ can be calculated by Eq. 1 as follows:

$$E_g = 1240/\lambda \quad (1)$$

where E_g is the band gap energy (eV) and λ is the wavelength (nm) of absorption edge in the spectrum. Accordingly, the band gap energy of $\text{Bi}_6\text{S}_2\text{O}_{15}$ is determined to be 3.36 eV, and the absorption edge is 369 nm

In absorption edge region of semiconductor, the square of absorption coefficient is liner with direct optical transition energy, whereas the square root of absorption coefficient linear with indirect optical transition energy.^{15,16} The insets of Fig. 2 shows the plots of absorption² versus energy and absorption^{1/2} versus energy in the absorption edge region. For $\text{Bi}_6\text{S}_2\text{O}_{15}$, the absorption² versus energy plot is nearly

liner, while the absorption^{1/2} versus energy deviates from the fitted straight line (Fig. 2). In our previous study,¹² we have demonstrated that Bi₂O(OH)₂SO₄ is direct optical transition and the band gap is determined to be 4.18 eV that is increased by 0.82 eV. In consideration of their same layered structures, we could hold that their greatly different absorption edges may be caused by hydroxyl. This has been further demonstrated as follows.

3.1.3 Effect on energy band and electron structures

The electronic structures of Bi₆S₂O₁₅ have been calculated by using the *Ab initio* density functional theory (DFT) calculations. The band structures of Bi₆S₂O₁₅ are shown in Fig. 3a. The Fermi energy, defined as the highest occupied energy level, has been taken as the valence band maximum (VBM); and the lowest unoccupied state is the conduction band minimum (CBM). For Bi₆S₂O₁₅, VBM and CBM are located at the *Z* point, further confirming the fact that Bi₆S₂O₁₅ is a direct band gap semiconductor. In our previous study,¹² Bi₂O(OH)₂SO₄ are demonstrated also to be a direct band gap. These results are all consistent with those revealed from the absorption spectra, as demonstrated above.

The total density of states (TDOS) and main partial density of states (PDOS) are shown in Fig. 3b. For Bi₆S₂O₁₅, the VB upper is mainly composed of O 2p orbital; while the CB bottom is composed of the Bi 6p. For Bi₂O(OH)₂SO₄, the previous study¹² has demonstrated the VB upper is mainly composed of O (bonding to S and H) 2p orbital; while the CB bottom is not only composed of Bi 6p, but also a little of H

1s orbital. The band gap of $\text{Bi}_6\text{S}_2\text{O}_{15}$ is determined to be 3.36 eV, E_{VB} and E_{CB} are determined to be 3.36 and 0 eV, respectively.¹⁶ While the band gap of $\text{Bi}_2\text{O}(\text{OH})_2\text{SO}_4$ is determined to be 4.18 eV, E_{VB} and E_{CB} are determined to be 4.39 and 0.21 eV, respectively.¹² Compared with the E_{VB} (3.36 eV) of $\text{Bi}_6\text{S}_2\text{O}_{15}$, that of $\text{Bi}_2\text{O}(\text{OH})_2\text{SO}_4$ is increased to 4.39 eV, which is induced by the O (bonding to H) 2p orbital of hydroxyl; whereas the E_{CB} (0.21 eV) of $\text{Bi}_2\text{O}(\text{OH})_2\text{SO}_4$ becomes more positive than that (0 eV) of $\text{Bi}_6\text{S}_2\text{O}_{15}$, which is induced by the H 1s orbital of hydroxyl. It is clear that hydroxyl has a significant influence on the energy band structure of semiconductor.

3.1.4 Effect on photocatalytic activity

Although the formulas and crystal structures of $\text{Bi}_6\text{S}_2\text{O}_{15}$ and $\text{Bi}_2\text{O}(\text{OH})_2\text{SO}_4$ are different, both of them have featured layered structures. The unit cell of $\text{Bi}_6\text{S}_2\text{O}_{15}$ is $(\text{Bi}_{12}\text{O}_{14})_n^{8n+}$ columns extending along the c axis, which are surrounded by eight tetrahedral SO_4^{2-} ; and $\text{Bi}_2\text{O}(\text{OH})_2\text{SO}_4$ consists of infinite $[\text{Bi}_2\text{O}(\text{OH})_2]_n^{2+}$ double chain and SO_4^{2-} . It is obvious that $\text{Bi}_2\text{O}(\text{OH})_2\text{SO}_4$ has a wider band gap than $\text{Bi}_6\text{S}_2\text{O}_{15}$ due to the hydroxyl (Fig. 4). To investigate the effect of hydroxyl on photocatalytic activity, the degradation activities and the reaction kinetic curves of $\text{Bi}_6\text{S}_2\text{O}_{15}$ and $\text{Bi}_2\text{O}(\text{OH})_2\text{SO}_4$ are evaluated for RhB under UV light irradiation ($\lambda \leq 420$ nm). Fig. 5a shows the photocatalytic activities of $\text{Bi}_6\text{S}_2\text{O}_{15}$ and $\text{Bi}_2\text{O}(\text{OH})_2\text{SO}_4$ for the degradation of RhB. After 50 min of irradiation, 87% and 44% of RhB have been degraded by $\text{Bi}_6\text{S}_2\text{O}_{15}$ and $\text{Bi}_2\text{O}(\text{OH})_2\text{SO}_4$, respectively. The $\text{Bi}_6\text{S}_2\text{O}_{15}$ shows a higher photocatalytic activity than the $\text{Bi}_2\text{O}(\text{OH})_2\text{SO}_4$. The apparent reaction rate constants

are determined to be 0.03972 and 0.01461 min^{-1} for $\text{Bi}_6\text{S}_2\text{O}_{15}$ and $\text{Bi}_2\text{O}(\text{OH})_2\text{SO}_4$, respectively (Fig. 5b). The apparent reaction kinetic rate of $\text{Bi}_6\text{S}_2\text{O}_{15}$ is 2.72 times higher than that of $\text{Bi}_2\text{O}(\text{OH})_2\text{SO}_4$. Fig. 5c shows the photoluminescence (PL) spectra of $\text{Bi}_6\text{S}_2\text{O}_{15}$ and $\text{Bi}_2\text{O}(\text{OH})_2\text{SO}_4$ under excitation wavelength of 248 nm. As indicated, both $\text{Bi}_6\text{S}_2\text{O}_{15}$ and $\text{Bi}_2\text{O}(\text{OH})_2\text{SO}_4$ show an intrinsic fluorescence emission peak at around 425 nm. The separation efficiency of the photogenerated electrons and holes can be investigated by PL.¹⁷ Generally, a low PL emission intensity indicates a low recombination efficiency of photogenerated charges, and thus a high photocatalytic activity. From Fig. 5c, $\text{Bi}_6\text{S}_2\text{O}_{15}$ sample shows an obviously lower emission intensity than $\text{Bi}_2\text{O}(\text{OH})_2\text{SO}_4$ sample. Moreover, electrochemical impedance spectroscopy (EIS) is measured to investigate the electron transfer rate (Fig. 5d). In the high frequency region of EIS Nyquist plot, the semicircle radius of $\text{Bi}_6\text{S}_2\text{O}_{15}$ is smaller than that of $\text{Bi}_2\text{O}(\text{OH})_2\text{SO}_4$. A smaller semicircle radius in EIS Nyquist plot means a smaller electric resistance of electrode. It is well-known that the separation efficiency of photoexcited electron-hole pairs is a crucial factor for the photocatalytic activity. A high conductivity of $\text{Bi}_6\text{S}_2\text{O}_{15}$ also favors for electron transportation, thus leading to an efficient charge separation. The result is in accordance with that from PL spectra.¹⁷ This is also in good agreement with their photocatalytic activities. The photocurrent shows the mobility of electrons generated in the photocatalyst, and the electronic transfer rate could directly correlate with the photocatalytic activity of material.¹⁸⁻¹⁹ The photocurrent of $\text{Bi}_6\text{S}_2\text{O}_{15}$ and $\text{Bi}_2\text{O}(\text{OH})_2\text{SO}_4$ samples (inset in Fig. 5d) generated in electrolyte under UV light. The photocurrent of $\text{Bi}_6\text{S}_2\text{O}_{15}$ electrode can

continuously generate while light-on, and its photocurrent density is greatly larger than that of $\text{Bi}_2\text{O}(\text{OH})_2\text{SO}_4$. These results are in accord with the order of photocatalytic activity, because the generation of photogenerated carriers is a crucial step of photocatalytic reaction. The band gap of $\text{Bi}_2\text{O}(\text{OH})_2\text{SO}_4$ is greatly expanded because of the introduction of hydroxyl. The UV-vis diffused reflectance spectra (DRS) shows that the absorption edge of $\text{Bi}_6\text{S}_2\text{O}_{15}$ is about 369 nm, corresponding to the band gap of 3.36 eV. Compared with $\text{Bi}_6\text{S}_2\text{O}_{15}$, the absorption edge and the highest absorption peak of $\text{Bi}_2\text{O}(\text{OH})_2\text{SO}_4$ are higher. However, both absorbance and band gap of $\text{Bi}_2\text{O}(\text{OH})_2\text{SO}_4$ are 296.6 nm and 4.18 eV, respectively; which may be induced by hydroxyl. The band gap of $\text{Bi}_2\text{O}(\text{OH})_2\text{SO}_4$ is wider than that of $\text{Bi}_6\text{S}_2\text{O}_{15}$, but the absorption of light is weaker than that of $\text{Bi}_6\text{S}_2\text{O}_{15}$. Therefore, the photocatalytic performance could result from the light absorption due to the wide band gap of $\text{Bi}_2\text{O}(\text{OH})_2\text{SO}_4$ induced by hydroxyl.

To elucidate the photocatalytic mechanisms of $\text{Bi}_6\text{S}_2\text{O}_{15}$ and $\text{Bi}_2\text{O}(\text{OH})_2\text{SO}_4$, the trapping experiments are performed to detect main oxidative species (radicals or holes) in the photocatalytic process. The holes (h^+) and hydroxyl radicals ($\bullet\text{OH}$) during the photodegradation of RhB over $\text{Bi}_6\text{S}_2\text{O}_{15}$ and $\text{Bi}_2\text{O}(\text{OH})_2\text{SO}_4$ are investigated with adding $(\text{NH}_4)_2\text{C}_2\text{O}_4\cdot\text{H}_2\text{O}$ (holes scavenger) and DMSO (hydroxyl radicals scavenger) (Fig. 6). In the $\text{Bi}_6\text{S}_2\text{O}_{15}$ system, the addition of DMSO only causes a small change in the photocatalytic degradation of RhB. On the contrary, the photodegradation of RhB is greatly reduced with adding $(\text{NH}_4)_2\text{C}_2\text{O}_4\cdot\text{H}_2\text{O}$, indicating that the holes are the main oxidative species of $\text{Bi}_6\text{S}_2\text{O}_{15}$ (Fig. 6a). In the $\text{Bi}_2\text{O}(\text{OH})_2\text{SO}_4$ system (Fig. 6b), the

photo catalytic degradation is slightly suppressed by the addition of $(\text{NH}_4)_2\text{C}_2\text{O}_4 \cdot \text{H}_2\text{O}$, while it is obviously inhibited when adding DMSO. These results above suggest that the main oxidative species transform from holes (h^+) to hydroxyl radicals ($\bullet\text{OH}$) from $\text{Bi}_6\text{S}_2\text{O}_{15}$ to $\text{Bi}_2\text{O}(\text{OH})_2\text{SO}_4$. It is obvious that the hydroxyl have widened the band gap and changed the position of VB and CB. Compared to $\text{Bi}_6\text{S}_2\text{O}_{15}$, $\text{Bi}_2\text{O}(\text{OH})_2\text{SO}_4$ has a positive CBM and VBM, which results in the transition of main oxidative species from hole (h^+) to hydroxyl radicals ($\bullet\text{OH}$) (Fig. 6). Moreover, the introduction of hydroxyl has expanded the band gap, which contributes to increasing the separation efficiency of photoinduced electron-hole pairs, but the band gap of $\text{Bi}_2\text{O}(\text{OH})_2\text{SO}_4$ is about 4.18 eV, which can only absorb light wavelength less than 296.6 nm, leading to the reduce of photocatalytic activity.

Efficient separation and transfer of photoinduced electrons and holes and the band gap structure greatly affect the photocatalytic oxidation of organic contaminants.²⁰ In the process of photocatalytic degradation, charge separation is important and necessary to prevent recombination of photoinduced electrons and holes. For $\text{Bi}_6\text{S}_2\text{O}_{15}$ and $\text{Bi}_2\text{O}(\text{OH})_2\text{SO}_4$, the featured layered configuration is considered to be very beneficial for the high photocatalytic activity.²¹ The internal electric fields are one of the most important parameters to evaluate the ability of electron-hole separation and transport in crystal lattice. Generally, the presence of internal electric fields between $[\text{Bi}_2\text{O}_2]$ and $[\text{SO}_4]$ is favorable for the efficient separation and transfer of photoinduced electrons and holes, which is also propitious to the high photocatalytic efficiencies for $\text{Bi}_6\text{S}_2\text{O}_{15}$ and $\text{Bi}_2\text{O}(\text{OH})_2\text{SO}_4$, but the band

gap of $\text{Bi}_2\text{O}(\text{OH})_2\text{SO}_4$ is too wider to absorb light wavelength less than 296.6 nm. As a result, the photocatalytic activity of $\text{Bi}_6\text{S}_2\text{O}_{15}$ has higher than that of $\text{Bi}_2\text{O}(\text{OH})_2\text{SO}_4$.

Summarily, although the photocatalytic activity of $\text{Bi}_2\text{O}(\text{OH})_2\text{SO}_4$ is not higher than that of $\text{Bi}_6\text{S}_2\text{O}_{15}$, the tuning strategy is useful and promising that we can facilely tune energy band of semiconductor by introducing or removing hydroxyl or the other anions so as to develop new photocatalysts. For example, most of visible light responsive photocatalysts (e.g., Fe_2O_3 , CuO , etc.) usually have lower photochemistry activities than ultraviolet light responsive ones. In particular, near-infrared light responsive semiconductors have fairly low or even have no photocatalytic activity (e.g., $\text{Cu}(\text{OH})\text{PO}_4$), which limits the utilization of solar energy. We can introduce hydroxyl or the other suitable anions to adjust appropriate energy bands of visible light responsive photocatalysts to develop a new photocatalyst with an improved activity; besides, for ultraviolet light responsive photocatalysts, the low utilization of solar energy is very low, which limits the practical application. We can remove anion from the appropriate anion to reduce band gap to develop new visible light responsive photocatalyst.

3.2 Morphology control of $\text{Bi}_2\text{O}(\text{OH})_2\text{SO}_4$

3.2.1 Influences of reaction temperature and medium

First, we investigated the influence of hydrothermal temperature on the sample. The hydrothermal temperature was varied from room temperature to 50, 70, 90, 110, 130, 150 and 170 °C, while the other processing parameters were kept same. At room

temperature, the irregular sample forms (Fig. 7a); at 50 °C, the sample consists of uniform microspheres of 40-45 μm in sizes (Fig. 7b); at 70 °C, the straw sheaves form, in which the nanoplates are about 700 nm thick (Fig. 7c); compared with that prepared at 70 °C, the sample at 90 °C shows the similar morphology, but its sizes (42-50 μm) are slightly larger than latter (Fig. 7d); at 110 °C, uniform flowers have formed, in which the nanoplates are about 500 nm thick (Fig. 7e); at 130 °C, the straw sheaves have also formed, of which the nanoplates are about 600 nm thick (Fig. 7f); at 150 °C and 170 °C, the samples are composed of plates and particles (Fig.s 7g and h). Fig. 7(i) shows their XRD patterns. In the temperature range of 50-130 °C, the phase-pure $\text{Bi}_2\text{O}(\text{OH})_2\text{SO}_4$ samples form, in agreement with the standard card (JCPDS 76-1102) (Fig. 7b-f). At 150 °C and 170 °C, the samples mainly consist of $\text{Bi}_2\text{O}(\text{OH})_2\text{SO}_4$, along with a small amount of impurities unknown. It is obvious that the reaction temperature has an important influence on the morphology and the crystalline phase of the products.

Secondly, the influence of reaction medium was also investigated on the sample. Fig. 8a demonstrates that the phase-pure $\text{Bi}_2\text{O}(\text{OH})_2\text{SO}_4$ can be achieved in glycerol, or ethylene glycol (EG), or ethanol. Moreover, the short rods form in ethanol, which are about 20 μm long (Fig. 8b). In EG, the straw sheaves are obtained, of which the nanoplates are about 700 nm thick (Fig. 8c). When glycerol is used as the medium, the formed flowers consist of numerous nanosheets (Fig. 8d). Our results have shown that the reaction medium has a significant influence on the particle morphology. Considering the different viscosities of ethanol ($\eta = 1.074 \text{ mPa s}$, 20 °C), ethylene

glycol ($\eta = 21 \text{ mPa s}$, $20 \text{ }^\circ\text{C}$) and glycerol ($\eta = 1412 \text{ mPa s}$, $20 \text{ }^\circ\text{C}$), we could assume that the viscosity of medium may affect the mobility or reactivity of ions, thus affecting crystal growth. Besides, it seems that the self-assembly process is favored by the medium molecules with hydroxyl groups (i.e. ethanol, ethylene glycol and glycerol). Herein, we could only assume that the surface adsorption of these molecules may occur, thus affecting the self-assembly process. In the present time, however, we can not provide a direct proof because of the system complexity. This needs further study in future.

Thirdly, we have also investigated the influence of the EG amount added on the samples. Herein, EG/H₂O volumetric ratio was varied from 2/3 to 1/1 and 3/2, while keeping the other preparation parameters same. The XRD patterns (Fig. 9a) indicate all the samples are phase-pure Bi₂O(OH)₂SO₄ at different amounts of EG added. At EG/H₂O=2/3, the sample is composed of (1.5-2)- μm -thick plates (Fig. 9b). The straw sheaves form at EG/H₂O=1/1, of which the nanoplates are about 700 nm thick (Fig. 9c and 9d). Typically, HRTEM is used to characterize the straw sheaves (Fig. 9e-g). The selected area electron diffraction pattern (SAED) reveals its single crystalline nature (Fig. 9f); and the lattice fringe image (Fig. 9g) demonstrates that the nanoplates grow preferentially along the [131] direction. At EG/H₂O=3/2, the flowers are obtained (Fig. 9h). It is obvious that reacting medium has a significant influence on the samples. It is well known that the viscosity of EG ($\eta = 21 \text{ mPa s}$, $20 \text{ }^\circ\text{C}$) is much higher than that of water ($\eta = 1.0087 \times 10^{-3} \text{ mPa s}$, $20 \text{ }^\circ\text{C}$). We could assume that a high EG content may lead to a slow mobility or reactivity of ions, which would affect crystal growth. The

fundamental physical and chemical interactions in our process need further investigation.

3.2.2 Influences of the addition amount of SO_4^{2-} and pH value

The effect of the amount of SO_4^{2-} added on the samples was mainly investigated while keeping the other experimental parameters constant. As shown in Fig. 4a, the XRD patterns of the samples can be well in agreement with the standard card (JCPDS 76-1102). At a low amount of Na_2SO_4 added (0.67mmol), the as-prepared sample consists of uniform microspheres with the diameters of 20-25 μm (Fig. 10b), of which the petals show a triangular shape and are about 700 nm thick. When the amount of Na_2SO_4 is increased to 1 and 1.5 mmol, the straw sheaves are obtained (Figs 10c and d). It seems that the SO_4^{2-} concentration has an important influence on the shapes and sizes of the sample. Herein we could assume that the straw sheaves may evolve from the splitting growth of the flowers. It has been reported²²⁻²⁷ that crystal splitting is associated with the fast crystal growth rate that is strongly dependent on the supersaturation of solution. As a result, the different SO_4^{2-} concentrations may result in different splitting degrees of crystals. According to the classical crystallography theory,²⁸ a large number of nuclei burst out rapidly at a high concentration of Na_2SO_4 . Generally, a lower monomer concentration favors isotropic growth, while a higher monomer concentration favors anisotropic growth.²⁹

Further, we have investigated the effect of pH value on the samples. Fig. 11a shows the XRD patterns of the products obtained at different amounts of HNO_3 added

(0 μL , 45 μL , 90 μL , 135 μL). All the XRD patterns can be well in agreement with the standard card (JCPDS 76-1102), but their crystallinities are not high. The straw sheaves form without adding HNO_3 , of which the nanoplates are about 700 nm thick (Fig. 11b). When 45 μL HNO_3 is added, the microspheres form (Fig. 11c). When the amount of HNO_3 is increased to 90 μL and 145 μL (Fig. 11d and e), the similar microspheres form, but their sizes are different (27 μm /90 μL , 33 μm /145 μL). Moreover, we have investigated the effect of the amount of ammonia ($\text{NH}_3\cdot\text{H}_2\text{O}$) added on the sample. Without adding $\text{NH}_3\cdot\text{H}_2\text{O}$ (Fig. 12a), the straw sheaves form, of which the nanoplate is about 700 nm thick. With the increase of adding the amount of $\text{NH}_3\cdot\text{H}_2\text{O}$ (45 μL and 90 μL), the straw sheaves grow continuously, but both ends of straw sheave (Fig.s 12b and c) become smaller. When 145 μL $\text{NH}_3\cdot\text{H}_2\text{O}$ is added (Fig. 12d), the nanoplate is about 500 nm thick and 10 μm long. Moreover, all the XRD patterns can be well in agreement with the standard card (JCPDS 76-1102) and the peak intensities increase with the amount of ammonia added (Fig. 12e). We assume that the pH value mainly affects the hydrolysis rate of Bi(III). With the increase of adding the amount of HNO_3 , the assembly becomes plump and tends to form microsphere. But with the increase of adding $\text{NH}_3\cdot\text{H}_2\text{O}$, the particles morphologies are similar but the size becomes smaller, so the pH value has an important influence on the morphologies.

3.2.3 Morphology-dependent photocatalytic activity

Fig. 13 shows the activity and reaction kinetic curves of three $\text{Bi}_2\text{O}(\text{OH})_2\text{SO}_4$

samples for the degradation of RhB dye under ultraviolet light irradiation ($\lambda \leq 420$ nm). The microspheres show a photocatalytic activity 1.3 and 2.2 times higher than long flakes and straw sheaves. We hold that the microsphere structure is beneficial to the reflection and absorption of light structure.¹⁵ After 150 min, 98% of RhB is evidently decolorized by microsphere, while only 25% of RhB degrade due to the photosensitization. Moreover, the apparent rate constant (k_a) of RhB by microsphere is 0.02 min^{-1} , which is 10 times higher than that without catalyst. Calculated by Scherer formulae, the average grain sizes of three samples are almost the same (Table 1). Moreover, the long flakes have a crystallinity slightly higher than straw sheaves and microspheres. However, the degradation rate of long flakes is 1.7 times as high as that of straw sheaves, which may be attributed to the high surface area (3.1 vs. $6.5 \text{ m}^2 \text{ g}^{-1}$) of long flakes. $\text{Bi}_2\text{O}(\text{OH})_2\text{SO}_4$ has a small solubility product value (1.8×10^{-31}) in water,²⁹ indicating a good stability in aqueous solution. Furthermore, we have investigated their stabilities by analyzing their XRD patterns before and after photocatalytic reaction (Fig. 14). Their crystallinities have nearly not changed, also confirming a high stability of $\text{Bi}_2\text{O}(\text{OH})_2\text{SO}_4$.

Moreover, electrochemical impedance spectroscopy (EIS) is used to investigate the electron transfer properties of $\text{Bi}_2\text{O}(\text{OH})_2\text{SO}_4$ (Fig. 15). In the high frequency region of Nyquist plot, the semicircle radius of microsphere is smaller than those of long flakes and straw sheaves. A smaller semicircle radius in the EIS Nyquist plot means a smaller electric resistance of electrode. It is well-known that the separation efficiency of photoexcited electron-hole pairs is a crucial factor for photocatalytic

activity. A high conductivity of microsphere also favors electron transport, leading to an efficient charge separation,^{30,31} so the microsphere has the highest photocatalytic activity.

4. Conclusions

Comparing $\text{Bi}_2\text{O}(\text{OH})_2\text{SO}_4$ with $\text{Bi}_6\text{S}_2\text{O}_{15}$ with the same layered structure, the introduction of hydroxyl leads to the significantly different band gaps (4.18 eV vs. 3.36 eV). The tuning strategy is useful and promising, new photocatalysts can be developed by introducing or removing hydroxyl and/or the other anions.

Supporting information

This supporting material can be free obtain via <http://www.elsevier.com>

Acknowledgments

This work is financially supported by National Science Foundation of China (21377060), Scientific Research Foundation for the Returned Overseas Chinese Scholars of State Education Ministry (2013S002), Six Talent Climax Foundation of Jiangsu (20100292), the Key Project of Environmental Protection Program of Jiangsu (2013005), “333” Outstanding Youth Scientist Foundation of Jiangsu (20112015), the Project Funded by the Science and Technology Infrastructure Program of Jiangsu (BM201380277), Jiangsu Science Foundation of China (BK2012862), Jiangsu Province of Academic Scientific Research Industrialization Projects (JHB2012-10),

and A Project Funded by the Priority Academic Program Development of Jiangsu Higher Education Institutions (PAPD) sponsored by SRF for ROCS, SEM (2013S002).

References

1. C. S. Pan and Y. F. Zhu, *Environ. Sci. Technol.*, 2010, **44**, 5570.
2. Z. G. Yi, J. H. Ye, N. K. Kikugawa, T. Kako, S. X. Ouyang, H. Stuart-Williams, H. Yang, J. Y. Cao, W. J. Luo, Z. S. Li, Y. Liu and R. L. Withers, *Nat. Mater.*, 2010, **9**, 559.
3. J. Wang, F. Teng, M. D. Chen, J. J. Xu, Y. Q. Song and X. L. Zhou, *CrystEngComm.*, 2013, **15**, 39.
4. M. Li, M. D. Chen, J. Wang and F. Teng, *CrystEngComm.*, 2014, **16**, 1237.
5. J. Li, L. Z. Zhang, Y. J. Li and Y. Yu, *Nanoscale*, 2014, **6**, 167.
6. Y. Zheng, F. Duan, M. Q. Chen and Y. Xie, *J. Mol. Catal. A: Chem.*, 2010, **317**, 34.
7. X. L. Fu, X. X. Wang, Z. X. Ding, D. Y. C. Leung, Z. Z. Zhang, J. L. Long, W. X. Zhang, Z. H. Li and X. Z. Fu, *Appl. Catal., B.*, 2009, **91**, 67.
8. T. J. Yan, J. L. Long, X. C. Shi, G. H. Wang, Z. H. Li and X. X. Wang, *Environ. Sci. Technol.*, 2010, **44**, 1380.
9. M. Sun, D. Z. Li, Y. Zheng, W. J. Zhang, Y. Shao, Y. B. Chen, W. J. Li and X. Z. Fu, *Environ. Sci. Technol.*, 2009, **43**, 7877.
10. H. W. Huang, Y. He, X. W. Li, M. Li, C. Zeng, F. Dong, X. Du, T. R. Zhang and Y.

- H. Zhang, *J. Mater. Chem. A*, 2015, **3**, 24547.
11. P. Mohapatra and K.M. Parida, *J. Mol. Catal. A-Chem.*, 2006, **258**, 118.
 12. H. Tian, F. Teng, J. Xu, S. Q. Lou, N. Li, Y. X. Zhao and M. D. Chen, *Sci. Rep.*, 2015, **5**, 7770.
 13. Y. Zhou, J. D. Grunwaldt, F. Krumeich, K. Zheng, G. Chen, J. Stötzel, R. Frahm and G. R. Patzke, *Small*, 2010, **6**, 1173.
 14. Y. Zhou and G. R. Patzke, *CrystEngComm.*, 2012, **14**, 1161.
 15. K. L. Zhang, C. M. Liu, F. Q. Huang, C. Zheng and W. D. Wang, *Appl. Catal., B.*, 2006, **68**, 125.
 16. J. Wang, W. J. Jiang, D. Liu, Z. Wei and Y. F. Zhu, *Appl. Catal., B.*, 2015, **176-177**, 306.
 17. Y. Wang, X. C. Wang and M. Antonietti, *Angew. Chem. Int. Ed.*, 2011, **50**, 2.
 18. G. G Zhang, M. W Zhang, X. X Ye, X. Q Qiu, S. Lin and X. C. Wang, *Adv. Mater.*, 2014, **26**, 805.
 19. H. Kim, P. Borse, W. Choi and J. Lee, *Angew. Chem., Int. Ed.*, 2005, **44**, 4585.
 20. Z. C. Shan, W. D. Wang, X. P. Lin, H. M. Ding and F. Q. Huang, *J. Solid State Chem.*, 2008, **181**, 1361.
 21. H. W. Huang, Y. He, Z. H. Lin, L. Kang and Y. H. Zhang, *J. Phys. Chem. C.*, 2013, **117**, 22986.
 22. K. Liu, H. P. You and G. Jia, *Cryst. Growth Des.*, 2010, **10**, 790.
 23. J. Tang and A. P. Alivisatos, *Nano Lett.*, 2006, **6**, 2701.
 24. K. Liu, Y. H. Zheng and G. Jia, *J. Solid State Chem.*, 2010, **183**, 2309.
 25. C. H. Lu, L. M. Qi, J. H. Yang, X. Y. Wang, D. Y. Zhang, J. L. Xie and J. M. Ma *Adv. Mater.*, 2005, **17**, 2562.

26. H. R. Zhang, C. M. Shen, S. T. Chen, Z. H. Xu, F. S. Liu, J. Q. Li and H. J. Gao, *Nanotechnol.*, 2005, **16**, 267.
27. J. P. Yang, F. C. Meldrum and J. H. Fendler, *J. Phys. Chem.*, 1995, **99**, 5500.
28. T. D. Nguyen and T. O. Do, *J. Phys. Chem. C.*, 2009, **113**, 11204.
29. C. Wu, L. Shen, Q. L. Huang and Y. C. Zhang, *Mater. Lett.*, 2011, **65**, 1134.
30. Z. L. Jiang, Y. X. Tang, Q. L. Tay, Y. Y. Zhang, O. I. Malyi, D. P. Wang, J. Y. Deng, Y. K. Lai, H. F. Zhou, X. D. Chen, Z. L. Dong and Z. Chen, *Adv. Mater.*, 2013, **3**, 1368.
31. X. Zhao, J. H. Qu, H. J. Liu and C. Hu, *Environ. Sci. Technol.*, 2007, **41**, 6802.

List of Tables and Fig.s

Table 1 Physicochemical properties of $\text{Bi}_2\text{O}(\text{OH})_2\text{SO}_4$ samples

Fig. 1. Crystal structure of (a) $\text{Bi}_6\text{S}_2\text{O}_{15}$ and (b) $\text{Bi}_2\text{O}(\text{OH})_2\text{SO}_4$

Fig. 2. UV-vis reflectance spectra (The inset shows the plots of absorption² vs. energy and absorption^{1/2} vs energy in the absorption edge region) of $\text{Bi}_6\text{S}_2\text{O}_{15}$: Circles for experimental data and the line for a linear fit

Fig. 3. Band structures (a), Total and partial DOS (b) of $\text{Bi}_6\text{S}_2\text{O}_{15}$

Fig. 4. Energy band positions of $\text{Bi}_6\text{S}_2\text{O}_{15}$ and $\text{Bi}_2\text{O}(\text{OH})_2\text{SO}_4$

Fig. 5. (a) Degradation curves and (b) reaction kinetic curves of RhB over $\text{Bi}_6\text{S}_2\text{O}_{15}$ nanowires and (c,d) $\text{Bi}_2\text{O}(\text{OH})_2\text{SO}_4$ microspheres under ultraviolet light irradiation ($\lambda \leq 420$ nm), (c) PL emission spectra, and (d) EIS plot and photocurrent-time dependence

Fig. 6. Degradation curves of RhB by $\text{Bi}_6\text{S}_2\text{O}_{15}$ (a) and $\text{Bi}_2\text{O}(\text{OH})_2\text{SO}_4$ (b) using different trapping chemicals under UV light irradiation ($\lambda \leq 420$ nm)

Fig. 7. Scanning electron microscopy (SEM) images (a-h) and X-ray diffraction (XRD) patterns (i) of the samples prepared at different temperatures while the other conditions are kept the same as those for straw sheaves: (a) Room temperature; (b) 50 °C; (c) 70 °C; (d) 90 °C; (e) 110 °C; (f) 130 °C; (g) 150 °C; (h) 170 °C

Fig. 8. SEM images and XRD patterns of the samples obtained at 90 °C for 12h with different reaction medium: (a) XRD patterns; (b) Ethanol; (c) Ethylene glycol; (d) Glycerol

Fig. 9. Effect of the added amount of ethylene glycol (EG) on the samples: (a) XRD pattern, (b) $\text{EG}/\text{H}_2\text{O} = 2/3$, (c,d) $\text{EG}/\text{H}_2\text{O} = 1/1$, (e) Transmission electron microscope of $\text{Bi}_2\text{O}(\text{OH})_2\text{SO}_4$ straw sheaves, (f) Selected area electron diffraction (SAED) of

$\text{Bi}_2\text{O}(\text{OH})_2\text{SO}_4$ straw sheaves, (g) Lattice fringe images of $\text{Bi}_2\text{O}(\text{OH})_2\text{SO}_4$ straw sheaves (h) $\text{EG}/\text{H}_2\text{O} = 3/2$

Fig. 10. Effect of the addition amount of SO_4^{2-} on the samples: (a) XRD patterns; (b) 0.67 mmol; (c) 1 mmol; (d) 1.5 mmol

Fig. 11. Effect of the added amount of 65 Wt.% HNO_3 on the samples: (a) XRD patterns; (b) Without HNO_3 , (c) 45 μL , (d) 90 μL , (e) 135 μL

Fig. 12. Effect of the added amount of 25~28 Wt.% ammonia on the samples: (a) without ammonia, (b) 45 μL ; (c) 90 μL ; (d) 135 μL ; (e) XRD patterns

Fig. 13. Degradation curves (a) and reaction kinetic curves (b) of RhB over $\text{Bi}_2\text{O}(\text{OH})_2\text{SO}_4$ samples

Fig. 14. X-ray diffraction patterns of $\text{Bi}_2\text{O}(\text{OH})_2\text{SO}_4$ samples: (A₁, A₂) Long flakes; (B₁, B₂) Straw sheaves; (C₁, C₂) Microspheres

Fig. 15. Nyquist plots of $\text{Bi}_2\text{O}(\text{OH})_2\text{SO}_4$ samples in 1 M Na_2SO_4 aqueous solution

Table 1

Sample	^[a] Crystallinity (%)	^[b] Average grain size (nm)	^[c] BET area (m ² g ⁻¹)
Long flakes	96.9	1.65	6.5
Straw sheaves	94.5	1.68	3.1
Microspheres	93.8	1.75	3.7

Notes: ^[a], calculated using jade software; ^[b], calculated by Scherrer formulae; ^[c], calculated by the Brunauer-Emmett-Teller (BET) method.

Fig. 1

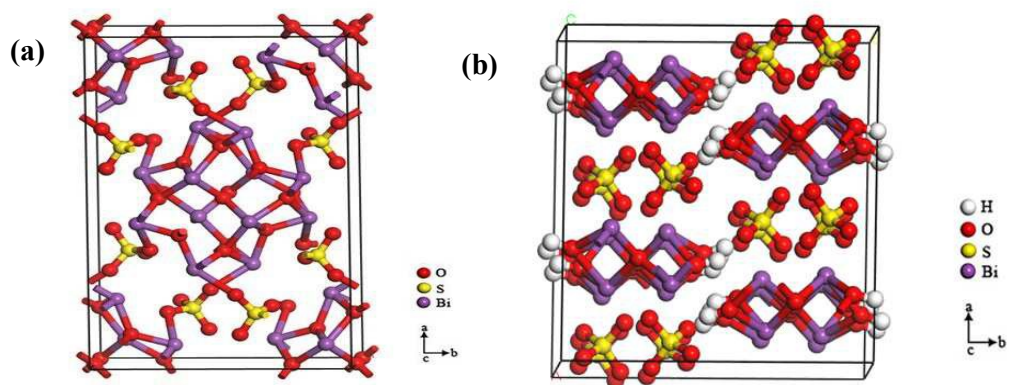


Fig. 2

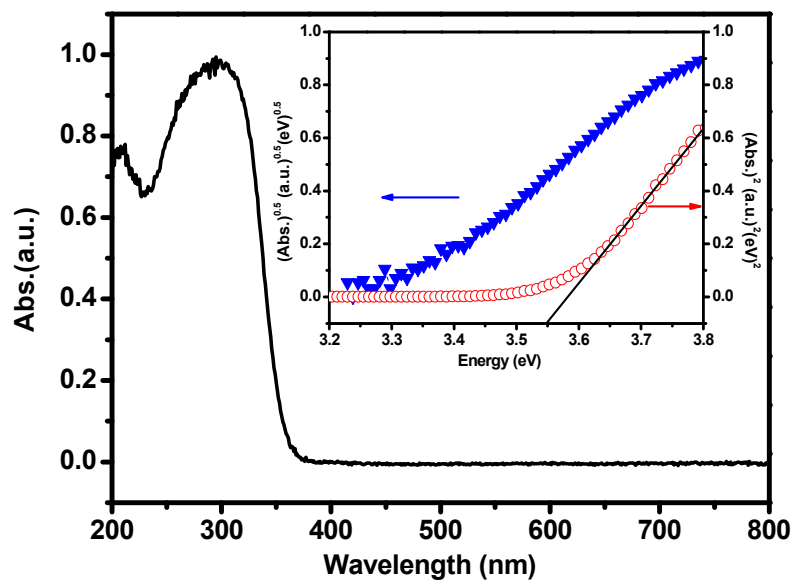


Fig. 3

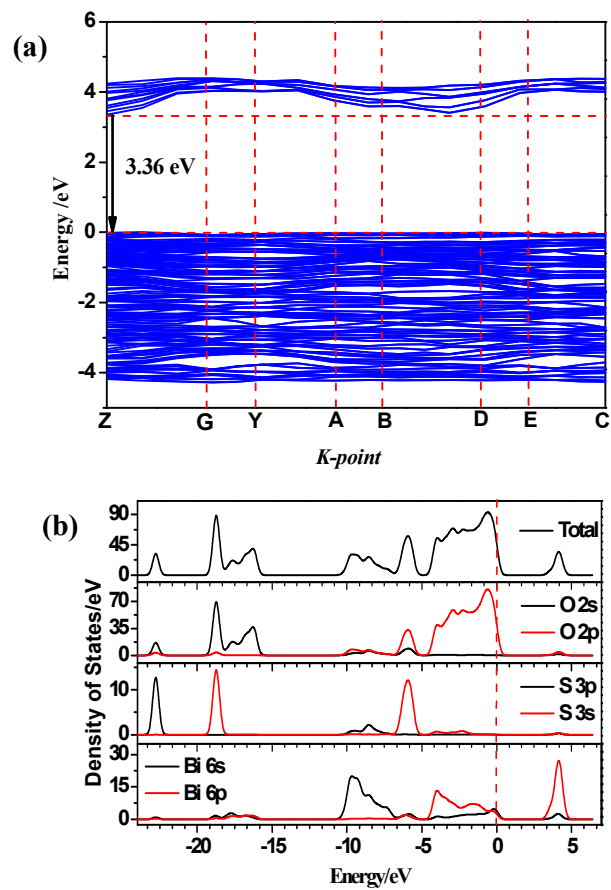


Fig. 4

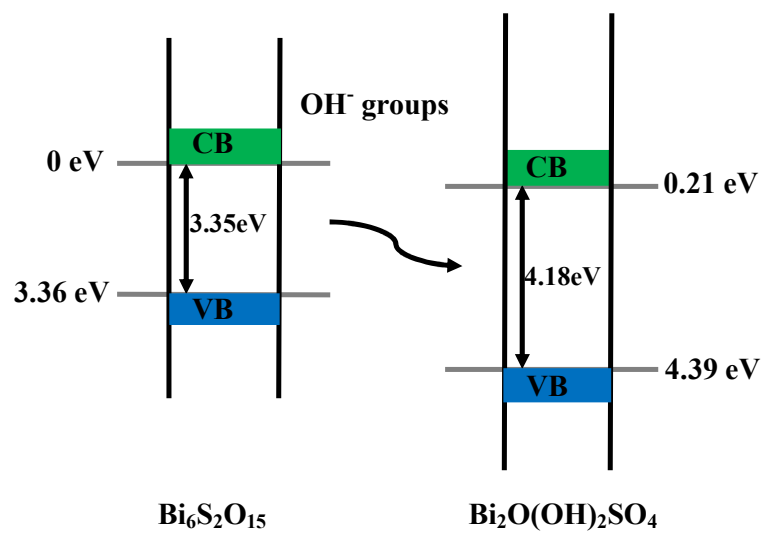


Fig. 5

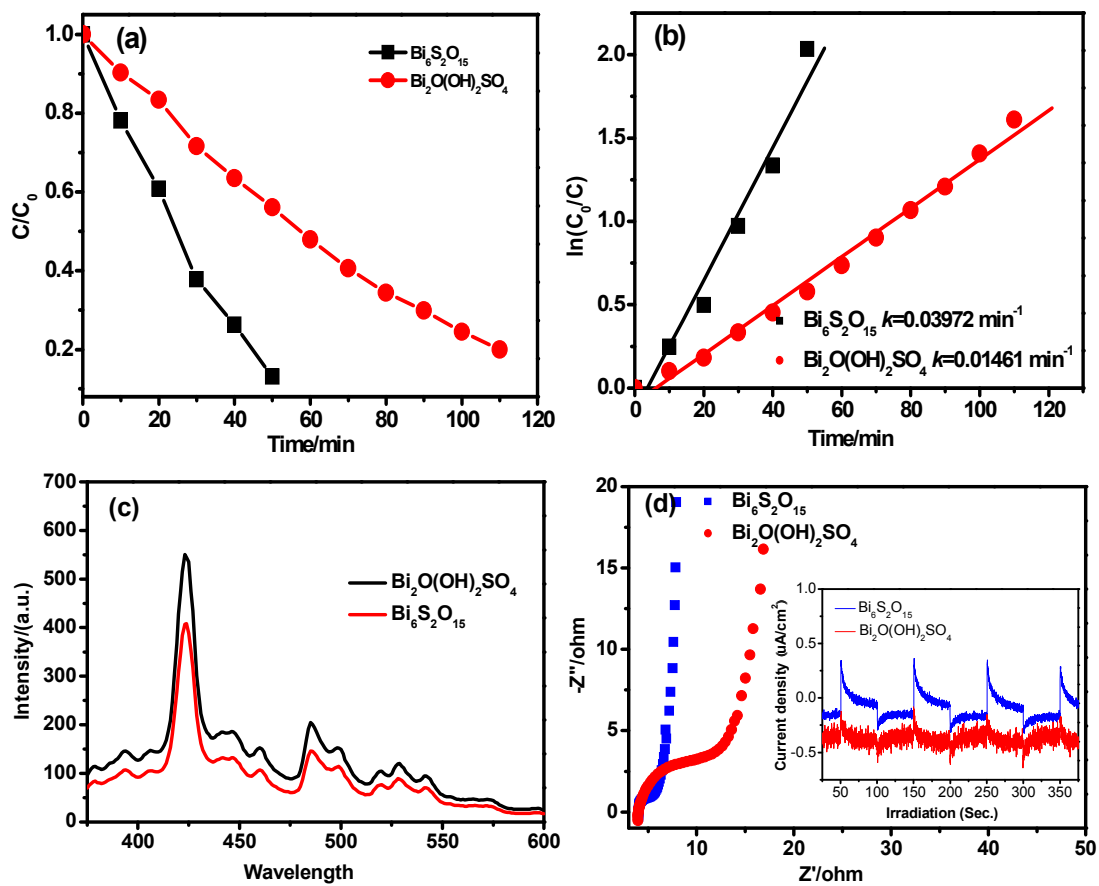


Fig. 6

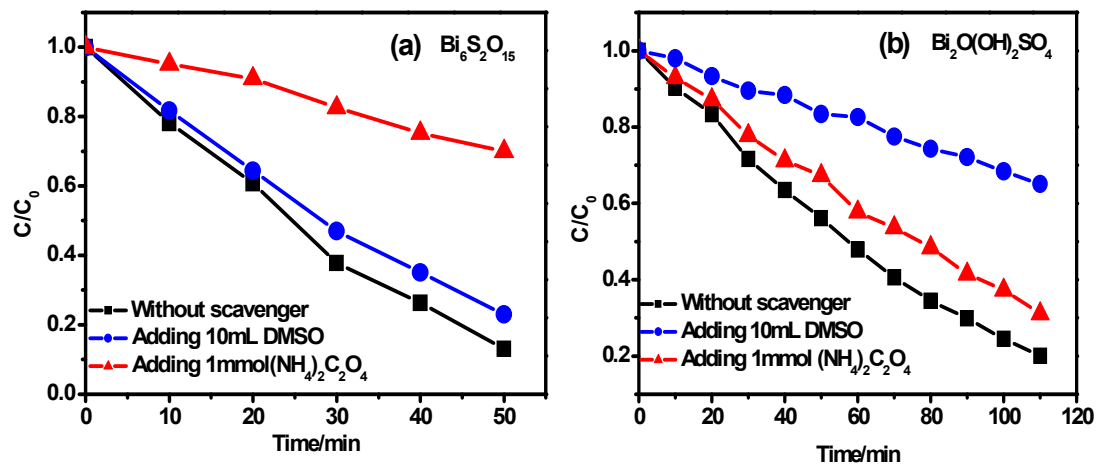
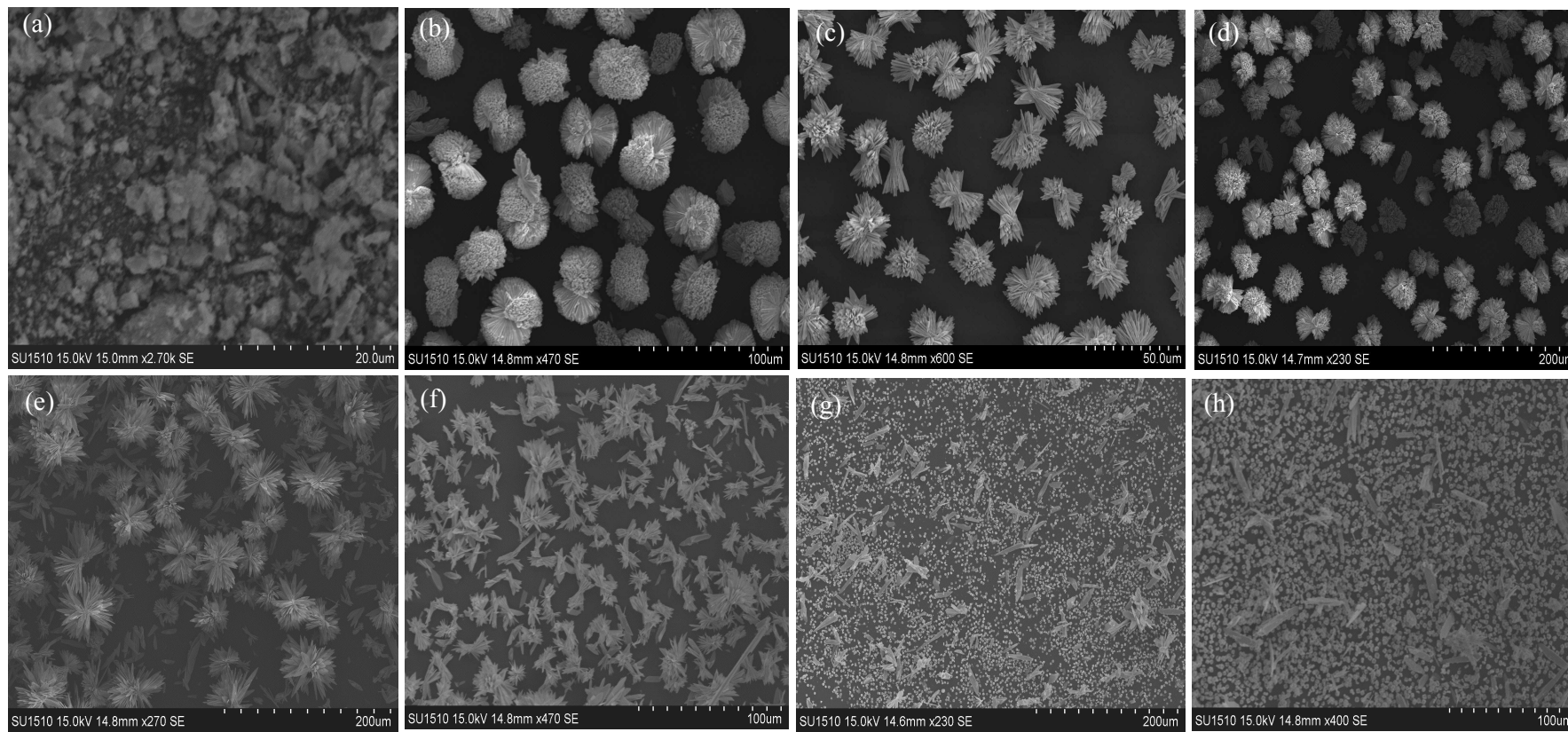


Fig. 7



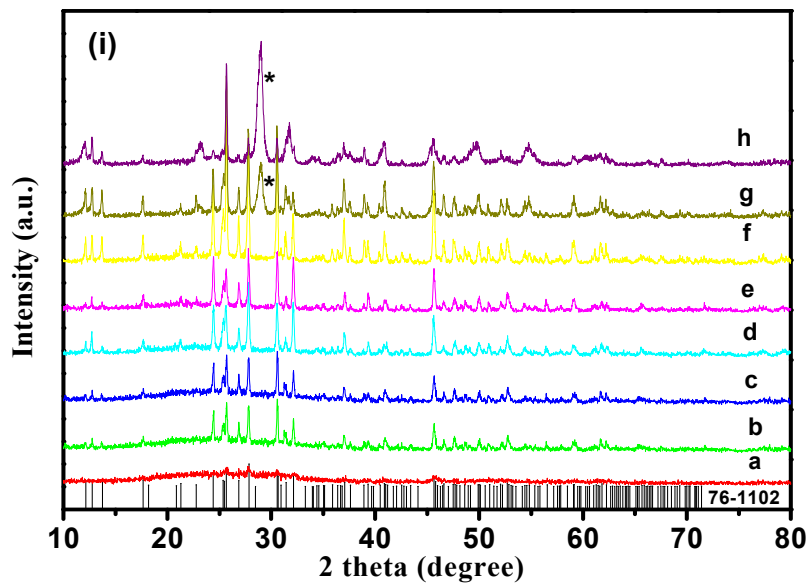


Fig. 8

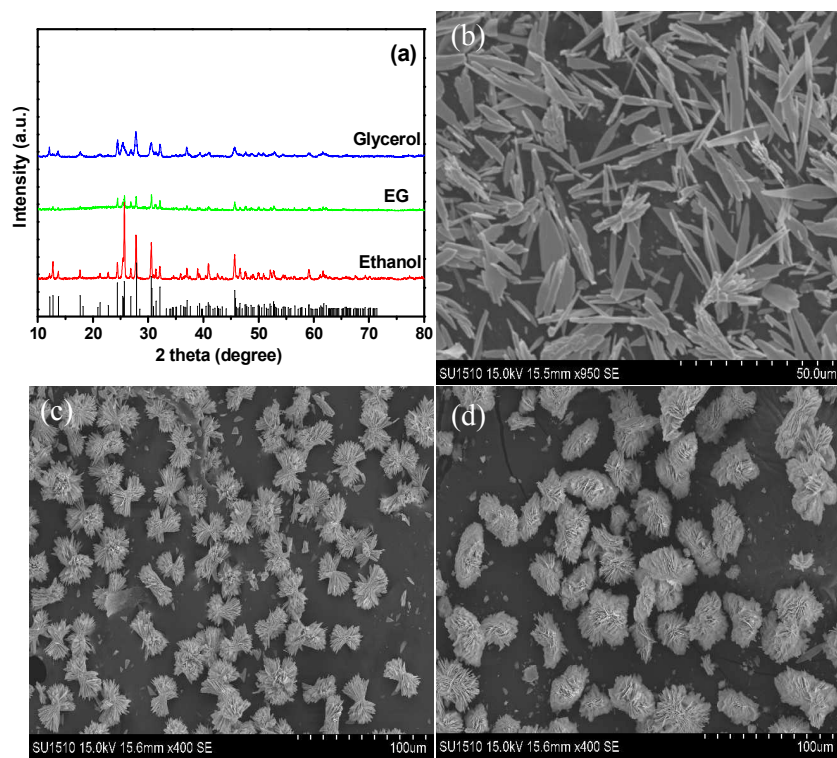


Fig. 9

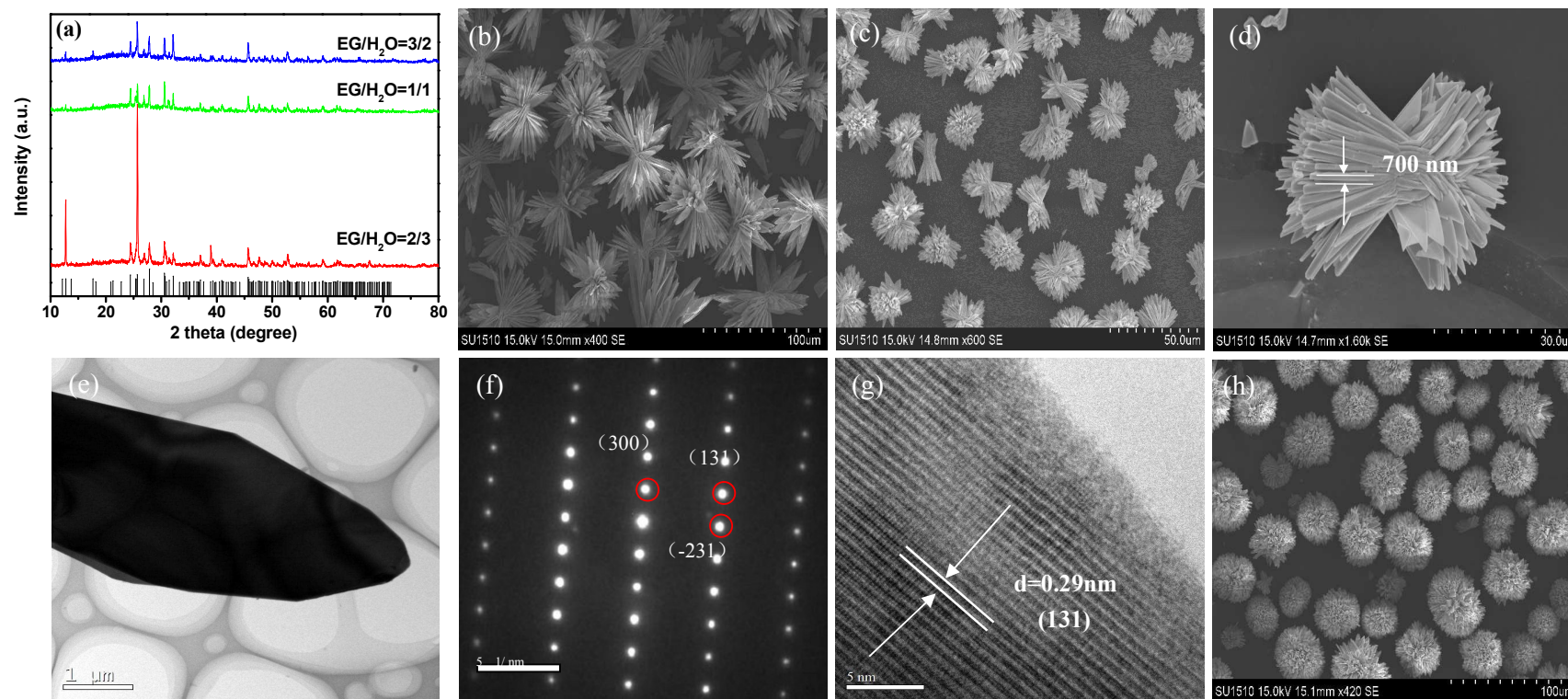


Fig. 10

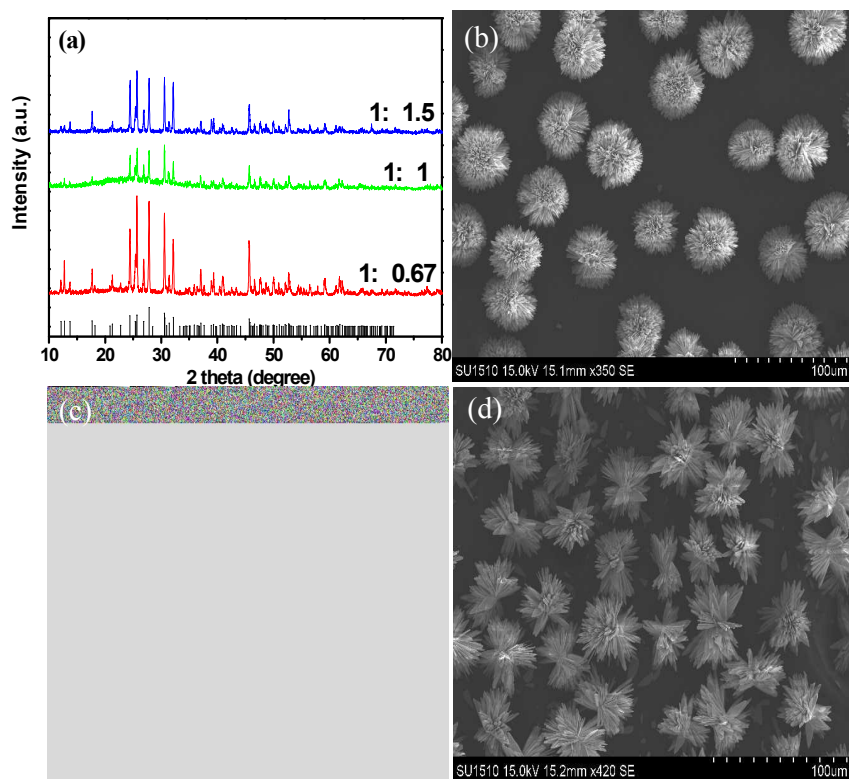


Fig. 11

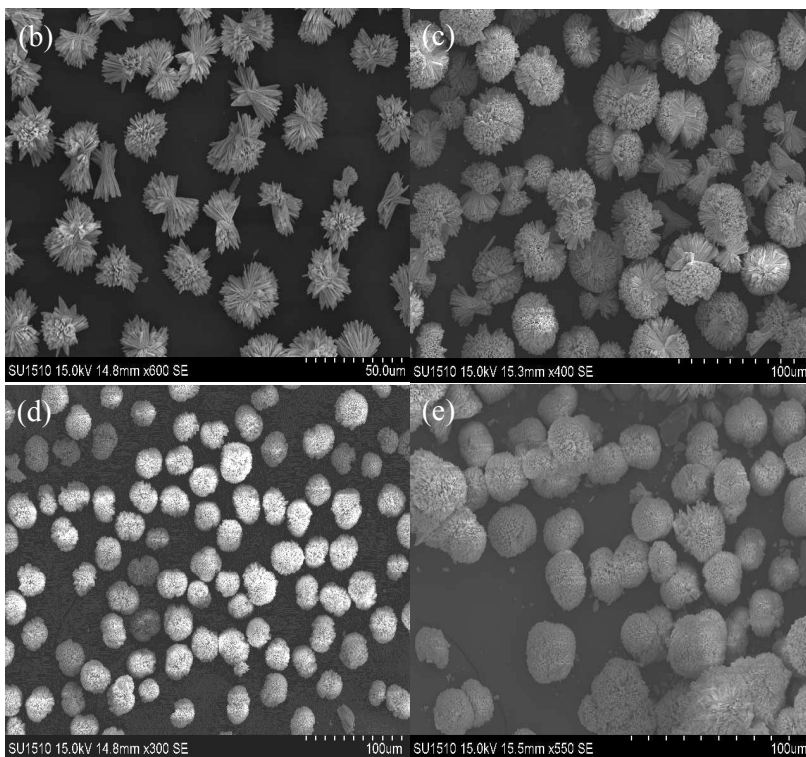
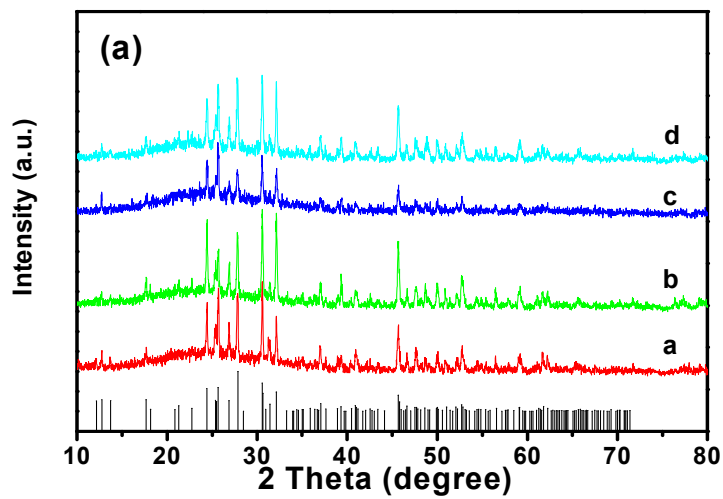


Fig. 12

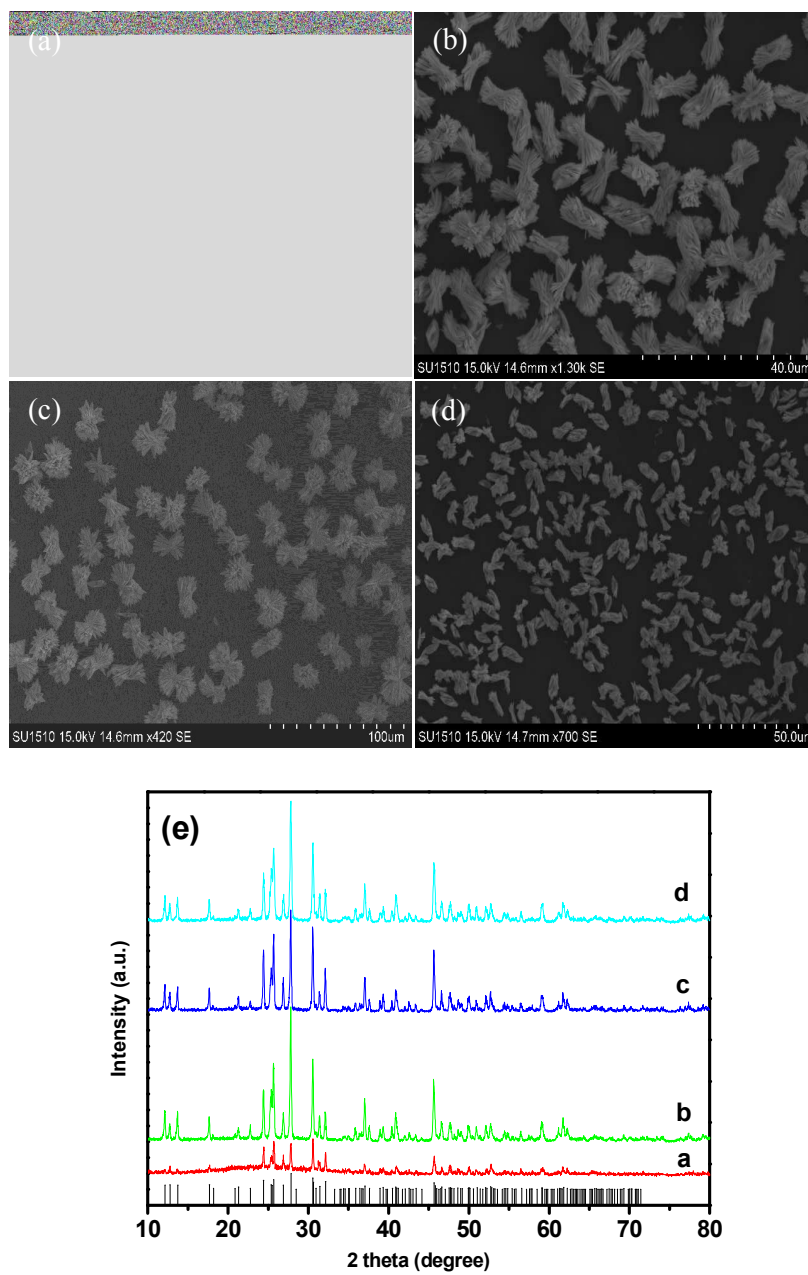


Fig. 13

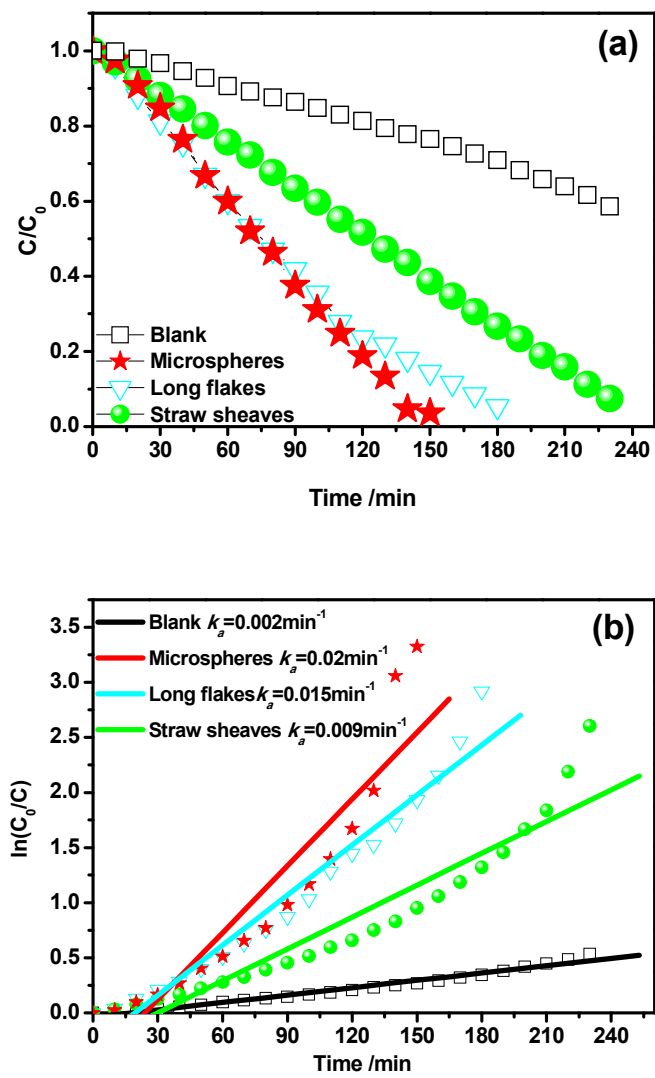


Fig. 14

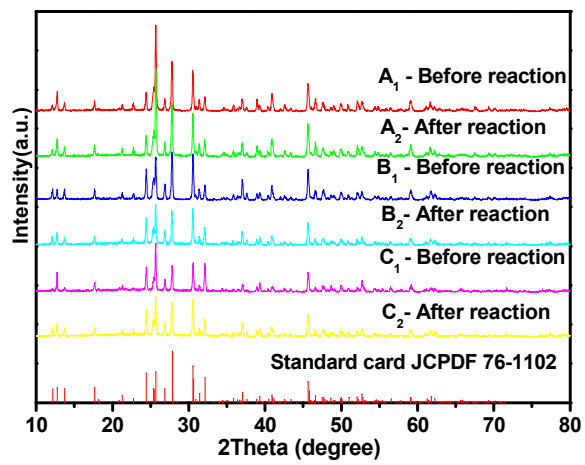
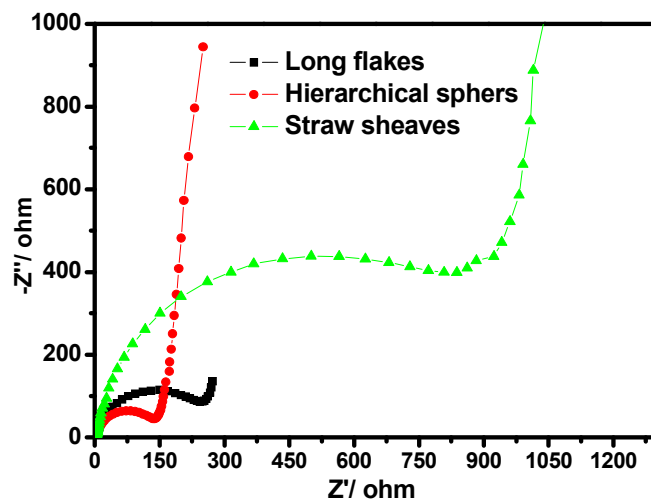
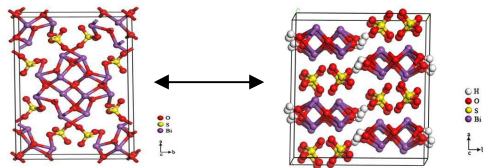


Fig. 15



Graphic Abstract

Energy band difference between $\text{Bi}_6\text{S}_2\text{O}_{15}$ with $\text{Bi}_2\text{O}(\text{OH})_2\text{SO}_4$ is mainly attributed to hydroxyl